



HAL
open science

SMOS-IC: an alternative SMOS soil moisture and 3 vegetation optical depth product

Roberto Fernández-Morán, Amen Al-Yaari, Arnaud Mialon, Ali Mahmoodi, Al Bitar Ahmad, Gabrielle de Lannoy, Ernesto Lopez-Baeza, Yann H. Kerr, Jean-Pierre Wigneron

► To cite this version:

Roberto Fernández-Morán, Amen Al-Yaari, Arnaud Mialon, Ali Mahmoodi, Al Bitar Ahmad, et al.. SMOS-IC: an alternative SMOS soil moisture and 3 vegetation optical depth product. 2017. hal-02787798

HAL Id: hal-02787798

<https://hal.inrae.fr/hal-02787798v1>

Preprint submitted on 5 Jun 2020

HAL is a multi-disciplinary open access archive for the deposit and dissemination of scientific research documents, whether they are published or not. The documents may come from teaching and research institutions in France or abroad, or from public or private research centers.

L'archive ouverte pluridisciplinaire **HAL**, est destinée au dépôt et à la diffusion de documents scientifiques de niveau recherche, publiés ou non, émanant des établissements d'enseignement et de recherche français ou étrangers, des laboratoires publics ou privés.



Distributed under a Creative Commons Attribution 4.0 International License

1 Article

2 **SMOS-IC: An alternative SMOS soil moisture and** 3 **vegetation optical depth product**

4 **Roberto Fernandez-Moran**^{1,2}, **Amen Al-Yaari**¹, **Arnaud Mialon**³, **Ali Mahmoodi**³, **Ahmad Al**
5 **Bitar**³, **Gabrielle De Lannoy**⁴, **Ernesto Lopez-Baeza**², **Yann Kerr**³, **Jean-Pierre Wigneron**¹

6 ¹ INRA, UR1391 ISPA, F-33140, Villenave d'Ornon, Centre INRA Bordeaux Aquitaine, France; amen.al-
7 yaari@inra.fr (A. A); jean-pierre.wigneron@inra.fr (J. -P. W)

8 ² University of Valencia. Faculty of Physics. Dept. of Earth Physics & Thermodynamics. Climatology from
9 Satellites Group. 46100 Valencia; Ernesto.Lopez@uv.es (E. L.)

10 ³ CESBIO, CNES/CNRS/IRD/UPS, UMR 5126, Toulouse, France; arnaud.mialon@cesbio.cnes.fr (A. M.);
11 mahmoodi.ca@gmail.com (A. M.); ahmad.albitar@cesbio.cnes.fr (A. A.); yann.kerr@cesbio.cnes.fr (Y. K.)

12 ⁴ KU Leuven, Department of Earth and Environmental Sciences, Heverlee, B-3001, Belgium;
13 (gabrielle.delannoy@kuleuven.be (G. D. L.)

14 * Correspondence: roberto.fernandez-moran@inra.fr; tel.: +33 7 52 04 30 85

15 **Abstract:** The main goal of the Soil Moisture and Ocean Salinity (SMOS) mission over land surfaces
16 is the production of global maps of soil moisture (SM) and vegetation optical depth (τ) based on
17 multi-angular brightness temperature (TB) measurements at L-band. The operational SMOS Level
18 2 and Level 3 soil moisture algorithms account for different surface effects, such as vegetation
19 opacity and soil roughness at 4 km resolution, in order to produce global retrievals of SM and τ . In
20 this study, we present an alternative SMOS product which was developed by INRA (Institut
21 National de la Recherche Agronomique) and CESBIO (Centre d'Etudes Spatiales de la Biosphère).
22 This SMOS-INRA-CESBIO (SMOS-IC) product provides daily SM and τ at the global scale and
23 differs from the operational SMOS Level 3 (SMOSL3) product in the treatment of retrievals over
24 heterogeneous pixels. Specifically, SMOS-IC is much simpler and does not account for corrections
25 associated to the antenna pattern and the complex SMOS viewing angle geometry. It considers
26 pixels as homogeneous to avoid uncertainties and errors linked to inconsistent auxiliary data sets
27 which are used to characterize the pixel heterogeneity in the SMOS L3 algorithm. SMOS-IC also
28 differs from the current SMOSL3 product (Version 300, V300) in the values of the effective
29 vegetation scattering albedo (ω) and soil roughness parameters. An inter-comparison is presented
30 in this study based on the use of ECMWF (European Center for Medium range Weather Forecasting)
31 SM outputs and NDVI (Normalized Difference Vegetation Index) from MODIS (Moderate-
32 Resolution Imaging Spectroradiometer). A 6 year (2010-2015) inter-comparison of the SMOS
33 products SMOS-IC and SMOSL3 SM (V300) with ECMWF SM yielded higher correlations and lower
34 ubRMSD (unbiased root mean square difference) for SMOS-IC over most of the pixels. In terms of
35 τ , SMOS-IC τ was found to be better correlated to MODIS NDVI in most regions of the globe, with
36 the exception of the Amazonian basin and of the northern mid-latitudes.

37 **Keywords:** SMOS; L-band; Level 3; ECMWF; SMOS-IC; soil moisture; vegetation optical depth;
38 MODIS; NDVI

39

40 **1. Introduction**

41 The estimation of surface soil moisture (SM) at global scale is a key objective for the recent L-
42 band (1.4 GHz) microwave missions SMOS (Soil Moisture and Ocean Salinity) (Kerr et al., 2012 [1])
43 and SMAP (Soil Moisture Active Passive) (Entekhabi et al., 2010 [2]). Measurements of soil moisture
44 are needed for applications related to the study of climate change or agriculture (droughts, floods,
45 etc.) and hydrological processes (Brocca et al., 2010 [3]) such as precipitation, infiltration, runoff and

46 evaporation. Moreover, SM is considered as an Essential Climate Variable and it is included in the
47 Climate Change Initiative (CCI) project (Hollmann et al., 2013 [4]).

48 The soil moisture of the first 2-3 cm soil layer is highly related to the soil emissivity at L-band
49 through the soil dielectric constant. SMOS uses an interferometric radiometer which delivers multi-
50 angular brightness temperature measurements at L-band (1.4 GHz). Currently, various products are
51 derived from the SMOS data at Level 2 (Kerr et al., 2012 [1]) and at Level 3 (Al Bitar et al., 2017 [5]),
52 such as the SMOSL3 Brightness Temperature (SMOSL3 TB) and the SMOSL3 SM and τ products,
53 with a 625 km² sampling. The SMOS SM retrieval algorithm, which is common to both SMOS Level
54 2 (L2) and Level 3 (L3) products, has been continuously improved since the launch of the satellite in
55 2009 (Kerr et al., 2001 [6]; Mialon et al., 2015 [7]; Al Bitar et al., 2017 [5]). It has been validated against
56 several datasets from various space-borne sensors (Al-Yaari et al., 2014 [8]; Al-Yaari et al., 2015 [9],
57 Kerr et al., 2016 [10]). All the different versions of the L2 and L3 products, are based on the inversion
58 of the L-band Microwave Emission of the Biosphere (L-MEB) radiative transfer model (Wigneron et
59 al., 2007 [11]), thus retrieving two main parameters, namely soil moisture and vegetation optical
60 depth at nadir (τ).

61 The SMOS τ is a measure of the attenuation of microwave radiation by the vegetation canopy at
62 L-band. Vegetation is commonly studied at optical or infrared frequencies. However, the longer
63 wavelength of L-band sensors allows penetration of the radiation within the canopy. Thus, τ can be
64 related to different vegetation features such as forest height (Rahmoune et al., 2013 [12], 2014 [13]),
65 vegetation structure (Schwank et al., 2005 [14], 2012 [15]), water content (Jackson and Schmugge, 1991
66 [16], Mo et al., 1982 [17], Wigneron et al., 1995 [18]; Grant et al., 2012 [19]), sapflow (Schneebeil et al.,
67 2011 [20]) and leaf fall (Guglielmetti et al., 2008 [21]; Patton et al., 2012 [22]). Furthermore, some
68 vegetation indices can also be related to τ such as the Leaf Area Index (LAI) (Wigneron et al., 2007
69 [11]) and the normalized difference vegetation index (NDVI) (Grant et al., 2016 [23]). Note that some
70 studies have also demonstrated the notable influence of soil roughness on the retrieved values of the
71 τ parameter at both local and regional scales (Patton et al., 2012 [22]; Fernandez-Moran et al., 2015
72 [24]; Parrens et al., 2017 [25]).

73 The L-MEB model has been progressively refined and improved (Wigneron et al., 2011 [26], in
74 press [27]). The SMOS L2 and L3 algorithms are based on a bottom-up approach where the TB
75 contributions of 4 x 4 km land cover surfaces are convoluted using the antenna pattern to upscale the
76 TB simulations to the sensor resolution. The use of such a bottom-up approach to retrieve SM and τ
77 presents two main drawbacks. First this approach is impacted by the uncertainties associated with
78 the higher resolution auxiliary files, like the land cover maps, which are used to characterize the pixel
79 heterogeneity. Second, the approach is more time consuming as the exact antenna patterns have to
80 be applied for each view angle.

81 In this study an alternative SMOS product is presented, hereinafter referred to as SMOS-IC. This
82 product is based on a simplified approach developed by INRA (Institut National de la Recherche
83 Agronomique) and CESBIO (Centre d'Etudes Spatiales de la Biosphère) and differs from the
84 operational SMOS Level 2 and Level 3 products in three main ways:

- 85 I. The SMOS-IC algorithm does not take into consideration pixel land use and assumes the
86 pixel to be homogeneous as suggested by Wigneron et al. 2012 [28]. The SM and τ retrieval
87 is performed over the whole pixel rather than over the fraction designated as either low
88 vegetation or forest. Note that this approach is similar to the one considered in the
89 development of the AMSR-E and SMAP SM algorithms (O'Neill et al., 2012 [25]). By
90 simplifying the retrieval approach, the SMOS-IC product becomes independent of the
91 ECMWF soil moisture information currently used as auxiliary information to estimate TB in
92 the subordinate pixel fractions of heterogeneous pixels in the operational SMOS L2 and L3
93 algorithms (Kerr et al., 2012 [1]).
- 94 II. SMOS-IC uses as input SMOS Level 3 fixed angle bins Brightness Temperature (TB) data
95 at the top of the atmosphere and contains different flags allowing to filter SM retrievals

96 accounting for the quality of the input TB data and for the TB angular range in the LMEB
97 inversion. SMOS-IC does not make use of the computationally expensive corrections based
98 on angular antenna patterns to account for pixel heterogeneity as in the L2 and L3 retrieval
99 algorithms.

100 III. New values of the effective vegetation scattering albedo (ω) and soil roughness parameters
101 (H_R , N_{RV} , and N_{RH}) are considered in the SMOS-IC product. This change is based on the
102 results of Fernandez-Moran et al. (2016) [29] who calibrated the L-MEB vegetation and soil
103 parameters for different land cover types based on the International Geosphere-Biosphere
104 Programme (IGBP) classes, as well as the findings of Parrens et al. (2016) [30] who
105 computed a global map of the soil roughness H_R values. The calibration of Fernandez-Moran
106 et al. (2016) [31] was obtained by selecting the values of the parameters (H_R , N_{RV} , N_{RH} , and
107 ω) which optimized the SMOS SM retrievals, with respect to the in situ SM values measured
108 over numerous sites obtained from ISMN. The parameter values resulting from this new
109 calibration differ from those used in the current SMOS L2 and L3 products. Values currently
110 used in the SMOS L2 and L3 algorithms (Kerr et al., 2012 [1]) were those decided before
111 launch from literature. Over forested areas, values were updated but not over low vegetation.
112 Consequently, in Version 620 of the L2 (and Version 300 for L3) algorithm, ω is still assumed
113 to be zero over low vegetation canopies and $\omega \sim 0.06 - 0.08$ over forests. Similarly, H_R is
114 equal to 0.3 for forests and $H_R = 0.1$ for the rest of the cover types, while Q_R is set to zero
115 whereas N_{RH} and N_{RV} are respectively set to 2 and 0 at global scale.

116 IV. In some cases, the Level 2 and Level 3 algorithms use values of LAI derived from MODIS
117 [32], to initialize the value of optical depth in the inversion algorithm (Kerr et al., 2012 [1]).
118 In SMOS-IC, this is not implemented, and the initialization of optical depth in the inversion
119 algorithm is based on a very simple approach (given in the following) and is completely
120 independent of the MODIS data.

121 An evaluation and calibration of SMOS-IC at local scale was performed in Fernandez-Moran et
122 al. (2016) [29]. The present study aims at presenting SMOS-IC and illustrating the main features of
123 the SMOS-IC SM and τ products at global scale, in comparison to the current SMOSL3 product. To
124 achieve this, the SMOS-IC and SMOSL3 SM products were compared against the ECMWF SM
125 product for ease of comparison. Furthermore, NDVI (Rouse et al., 1974 [33]) from the Moderate-
126 Resolution Imaging Spectroradiometer (MODIS) was used as a vegetation index to analyze the
127 seasonal changes in the τ products from both SMOS-IC and SMOSL3. The NDVI index which is
128 derived from optical observations cannot be directly compared to the τ product, which is derived
129 from microwave observations. However, the NDVI index is a good indicator of the vegetation density
130 and it can be used to interpret the seasonal changes in the SMOS τ product at large scale as found by
131 Grant et al. (2016) [23], but with some caveats: saturation effects at high levels of vegetation density,
132 sensitivity to the effects of snow and soil reflectivity (Qi et al., 1994 [34]), etc. It may be noted that
133 NDVI is the proxy used for estimating τ in the current operational algorithm of the SMAP mission
134 (O'Neill et al., 2012 [35]).

135 In section 2, we present a description of both SMOS algorithms (SMOSL3 and SMOS-IC) and of
136 the MODIS NDVI and ECMWF SM data sets. The inter-comparison of the SMOS products in terms
137 of soil moisture and vegetation optical depth is given in section 3. The inter-comparison covers almost
138 6 years of data, from 2010 to 2015, excluding the commissioning phase (the first six months of 2010;
139 Corbella et al., 2011 [36]). Discussion and conclusions are presented in section 4.

140 2. Materials and method

141 2.1 SMOSL3 brightness temperature, soil moisture and vegetation optical depth

142 At Level 3, there are different SMOS products (Al Bitar et al., 2017 [5]). In this study we used the
 143 SMOS L3 products which include TB, τ and SM (version 300) data produced by the CATDS (Centre
 144 Aval de Traitement des Données SMOS) (Al Bitar et al., 2017 [5]). These products are available in the
 145 NetCDF format and on the Equal-Area Scalable Earth (EASE) 2.0 grid (Armstrong et. al, 1997 [37])
 146 with a 625 km² sampling (Brodzik and Knowles, 2002 [38]). The SMOSL3 TB is measured at the top
 147 of the atmosphere and provided in the surface reference frame (i.e., H and V polarizations) at angles
 148 ranging from $2.5^\circ \pm 2.5^\circ$ to $62.5^\circ \pm 2.5^\circ$. Ascending ($\sim 06:00$ LST at the equator) and descending ($\sim 18:00$
 149 LST) orbits are processed separately. The Level 3 processor uses the same physically based forward
 150 model (L-MEB) as the ESA SMOS Level 2 processor (Kerr et al., 2012 [1], Kerr et al., 2013 [39]) for the
 151 retrieval of both SM and τ from dual polarization (H, V) and multi-angular SMOS measurements.
 152 The retrieval algorithm consists of the minimization of the differences between observed and
 153 modeled Level 1 TB (through the L-MEB forward model) in a Bayesian cost function which accounts
 154 for the observation uncertainty, and also contains a prior parameter constraint. One of the
 155 characteristics of the TB modeling is the consideration of surface heterogeneity. The total modeled
 156 TB is simulated as the sum of TB contributions from several fractions (nominal or low vegetation,
 157 forest, and others as urban, water, etc.). In most of the cases, the SM retrieval is estimated from the
 158 TB contribution which corresponds to areas with low vegetation (nominal fraction), while the TB
 159 forest contribution is computed using ancillary data such as ECMWF SM. In other cases, the retrieval
 160 is performed entirely over the forest fraction. Dynamic changes as freezing or rainfall events are
 161 considered through ancillary weather data from ECMWF.

162 The SMOSL3 τ and SM retrievals are provided at different temporal resolutions: daily, 3-days,
 163 10-days, and monthly averaged (Kerr et al., 2013 [39]; Jacquette et al., 2010 [40]). The quality of the
 164 SMOSL3 product containing SM and τ data is improved by the use of multi-orbit retrievals (Al Bitar
 165 et al., 2017 [5]). The SMOS ascending (6 am LST) and descending (6 pm LST) orbits are processed
 166 separately in this product in order to better account for the diurnal effects (surface, Total Electron
 167 Content which drives Faraday rotation and sun corrections) and, in some areas, Radio Frequency
 168 Interferences (RFI) effects (Oliva et al., 2012 [41]) and sun glint impacts at L-band (Khazâal et al., 2016
 169 [42]).

170 In SMOS-IC, we used the SMOS L3 TB product as input to the inversion algorithm. This product,
 171 which includes many corrections, is very easy and convenient to use (conversely, the L2 and L3
 172 algorithms are based on L1 C TB data).

173 2.2 SMOS-IC soil moisture and vegetation optical depth dataset

174 2.2.1 Model description

175 As for the L2 and L3 algorithms, in SMOS-IC, the retrieval of the soil moisture and vegetation
 176 optical depth at nadir is based on the L-MEB model inversion (Wigneron et al., 2007 [11]). The
 177 retrieval is performed over pixels which are considered as entirely homogeneous; in other words, a
 178 single representative value of each input model parameter is used for the whole pixel.

179 In L-MEB, the simulation of the land surface emission is based on the τ - ω radiative transfer
 180 model (Mo et al., 1982 [17]) using simplified (zero-order) radiative transfer equations. The model
 181 represents the soil as a rough surface with a vegetation layer. The modeled TB from the soil vegetation
 182 medium is calculated as the sum of the direct vegetation emission, the soil emission attenuated by
 183 the canopy and the vegetation emission reflected by the soil and attenuated by the canopy following
 184 equation (1). The atmospheric contribution is neglected.

$$185 \quad TB_P(\theta) = (1 - \omega)[1 - \gamma_P(\theta)][1 + \gamma_P(\theta)r_{GP}(\theta)]T_C + [1 - r_{GP}(\theta)]\gamma_P(\theta)T_G$$

186 (1)

187 where θ is the incidence angle, r_{GP} is the soil reflectivity, T_G and T_C are the soil and canopy
 188 effective temperatures, γ_p is the vegetation transmissivity (or vegetation attenuation factor) and ω
 189 is the effective scattering albedo (polarization effects are not taken into account for this parameter).

190 Roughness effects are parameterized through a semi-empirical approach initially developed by
 191 Wang and Choudhury (1981) [43] and refined in more recent studies (Escorihuela et al., 2007 [44];
 192 Lawrence et al., 2013 [45]; Parrens et al., 2016 [25]). The roughness modelling is based on four
 193 parameters (Q_R , H_R , N_{RH} and N_{RV}). The values of Q_R and N_{RP} ($P = H, V$) have been calibrated in
 194 Fernandez-Moran et al. (2015, 2016) [46][29] where optimized values of $Q_R = 0$ and $N_{RP} = -1$ ($p = H, V$)
 195 were obtained globally. Thus, the calculation of the soil reflectivity r_{GP} is given by:

$$196 \quad r_{GP}(\theta) = r_{GP}^*(\theta)\exp[-H_R/\cos(\theta)] \quad (2)$$

197 where r_{GP}^* ($P = H, V$) is the reflectivity of a plane (specular) surface, which is computed from
 198 the Fresnel equations (Ulaby, 1982 [47]) as a function of θ and of the soil dielectric constant (ϵ),
 199 expressed as a function of SM, soil clay fraction and soil effective temperature (T_G) using the model
 200 developed by Mironov et al. (2012) [48]. H_R accounts for the decrease of r_{GP} due to soil roughness
 201 effects.

202 Under the assumption of isotropic conditions and no dependence of the vegetation optical depth
 203 on polarization, the vegetation attenuation factor γ_p can be computed using the Beer's law as:

$$204 \quad \gamma_p = \exp[-\tau/\cos(\theta)] \quad (3)$$

205 The retrieval of SM and τ involves the minimization of the following cost function x :

$$206 \quad x = \frac{\sum_{i=1}^N (TB_p(\theta)_{mes} - TB_p(\theta))^2}{\sigma(TB)^2} + \sum_{i=1}^2 \frac{(P_i^{ini} - P_i)^2}{\sigma(P_i)^2} \quad (4)$$

207 where N is the number of observations for different viewing angles (θ) and both polarizations
 208 (H & V), $TB_p(\theta)_{mes}$ is the measured value over the SMOS pixels from the SMOSL3 TB product
 209 (presented in section 2.2.2), $\sigma(TB)$ is the standard deviation associated with the brightness
 210 temperature measurements (this parameter was set to the constant value of 4 K in this study), $TB_p(\theta)$
 211 is the brightness temperature calculated using equation (1), P_i ($i = 1, 2$) is the value of the retrieved
 212 parameter (SM, τ); P_i^{ini} ($i = 1, 2$) is an *a priori* estimate of the parameter P_i ; and $\sigma(P_i)$ is the standard
 213 deviation associated with this estimate. A constant initial value of $0.2 \text{ m}^3/\text{m}^3$ was considered for SM
 214 and $\sigma(SM)$ and a value of 0.5 was considered for τ_{NAD} and 1 for $\sigma(\tau_{NAD})$.

215 2.2.2 Effective vegetation scattering albedo, soil roughness and soil texture parameters

216 One of the most important features of the SMOS-IC product is the ability to test new calibrated
 217 values of ω (Fernandez-Moran et al, 2016 [29]) and H_R (Parrens et al. 2016 [30]). Table 1 presents these
 218 values for SMOS-IC and SMOSL3 V300 as a function of the IGBP land category classes. It must be
 219 noted that SMOSL3 V300 uses the ECOCLIMAP classification (Masson et al., 2003 [49]) and that in
 220 new versions of SMOSL3, IGBP land use maps could be used.

221 Table 1: Calibrated values of ω and H_R as function of the IGBP land category classes for SMOS-IC and
 222 SMOSL3.

Class	ω (SMOS-IC)	ω (SMOSL3 V300)	H_R (SMOS-IC)	H_R (SMOSL3 V300)
1 – Evergreen needle leaf forest	0.10	0.06 – 0.08*	0.30	0.30

2 – Evergreen broadleaf forest	0.10	0.06 – 0.08*	0.47	0.30
3 – Deciduous needle leaf forest	0.10	0.06 – 0.08*	0.43	0.30
4 – Deciduous broadleaf forest	0.10	0.06 – 0.08*	0.46	0.30
5 – Mixed forests	0.10	0.06 – 0.08*	0.43	0.30
6 – Closed shrublands	0.10	0.00	0.27	0.10
7 – Open shrublands	0.08	0.00	0.17	0.10
8 – Woody savannas	0.12	0.00	0.35	0.10
9 – Savannas	0.10	0.00	0.23	0.10
10 – Grasslands	0.10	0.00	0.12	0.10
11 – Permanent wetland	0.10	0.00	0.19	0.10
12 – Croplands	0.12	0.00	0.17	0.10
13 – Urban and built-up	0.10	0.00	0.21	0.10
14 – Cropland/Natural Vegetation Mosaic	0.12	0.00	0.22	0.10
15 – Snow and ice	0.10	0.00	0.12	0.10
16 – Barren and sparsely vegetated	0.12	0.00	0.02	0.10

223 * $\omega = 0.08$ over boreal forests, $\omega = 0.06$ over other forest types

224 In SMOS-IC, the retrieval of SM and τ is performed over the totality of each pixel and the input
 225 parameters H_R and ω are consequently constant values for the whole pixel. However, due to the
 226 heterogeneity present in all pixels, the input H_R and ω parameters used in the retrieval are calculated
 227 by linear weighting the H_R and ω contribution according to the percentage of each IGBP class within
 228 the pixel based on the values provided in Table 1. For instance, if a pixel is covered by 60% of
 229 grasslands and 40% of croplands, the effective vegetation scattering albedo considered for that pixel
 230 is calculated as follows: $\omega = 0.60 \cdot 0.10 + 0.40 \cdot 0.12 = 0.108$. The assumption of linearity, which is
 231 questionable, was made here as it leads to a very simple correction, and as no other more physical
 232 and general formulation was available.

233 The soil texture in terms of clay content is obtained in the SMOS-IC product from the Food and
 234 Agriculture Organization map (FAO, 1998) [50]. This map is re-gridded in the same EASE 2.0 grid
 235 used by SMOSL3.

236 2.2.3 Quality flags

237 The data filtering of the SMOS-IC product was done through different scene and quality flags
 238 which are summarized in Tables 2 and 3. The scene flags indicate the presence of moderate and strong
 239 topography, frozen soil or polluted scene. TB data for pixels where the sum of the water, urban and
 240 ice fractions were higher than 10% were filtered out (considered as polluted scene). For ECMWF soil
 241 temperatures below 273.15 K, the soil was considered as frozen. The quality flags helped to filter out
 242 all cases suspected to give dubious results. Consequently, only TB values not affected by noise (RFI,
 243 Sun glint effects, etc) were selected. For this, only TB values whose standard deviations were within
 244 radiometric accuracy were kept (TB with a standard deviation exceeding 5 K plus the TB radiometric
 245 accuracy were filtered out). Moreover, only retrievals (i) made in the range of incidence angles of 20
 246 to 55° and (ii) with a range of angular values exceeding 10° (to ensure a sufficient sampling of the
 247 angular distribution) were considered. The quality flags helped also to filter out those retrievals

248 where the RMSE values between the measured (L3 TB) and the L-MEB modeled TB data were larger
249 than 12 K as suggested in Wigneron et al. (2012) [28].

250 Table 2: Description of the SMOS-IC scene flags

Scene flags	Description
Presence of moderate topography	Same filter as SMOSL3 V300
Presence of strong topography	Same filter as SMOSL3 V300
Polluted scene	Water, urban and ice fractions (according to the IGBP classification) represent less than 10% of the pixel
Frozen scene	Soil temperature < 273.15 K

251

252 Table 3: Description of the SMOS-IC quality flags

Quality flags	Description
SM retrieved successfully	
SM retrieved successfully but not recommended	RMSE < 12 K
No data after first filtering	TB not valid (angles out of the range 20–55°); TB standard deviation higher than accuracy + 5 K
Failed retrieval (1)	TB angle separation too narrow (angle difference < 10°)
ECMWF soil temperatures out of range	“No value” or values out of range
Failed retrieval (2)	Values of clay content are out of range
Failed retrieval (3)	SM < 0 m ³ /m ³

253

254 2.3 ECMWF and MODIS data

255 The ECMWF dataset used in this study for the SM product inter-comparison was obtained from
256 the SMOSL3 SM pre-processor. This ECMWF product has a spatial resolution of 625 km² and 1-day
257 temporal resolution, using the same EASE 2.0 grid and interpolated in time and space to fit the
258 SMOSL3 sampling resolutions. It is based on the ERA-Interim dataset. ERA-Interim uses a numerical
259 weather prediction (NWP) system (IFS – Cy31r2) to produce reanalyzed data (Berrisford et al., 2011)
260 [51].

261 The ECMWF soil surface (Level 1, top 0-7 cm soil layer) and soil deep temperature (Level 3, 28-
262 100 cm) are used in the computation of the effective soil temperature for the SMOS-IC and SMOSL3
263 SM products following the parameterization of Wigneron et al. (2001) [52]. It is worth noting that unlike
264 the SMOSL3 SM product, the SMOS-IC processor does not use the ECMWF SM product to compute
265 contributions from the fixed fractions (i.e. fraction of the scene over which the SM retrieval is not performed),
266 and is only considered for evaluation purpose in this study.

267 The ECMWF SM product represents the top 0-7 cm surface layer and it has been frequently
268 compared to retrieved SM at global scale (Al-Yaari et al., 2014 [53]; Albergel et al., 2013 [54]; Leroux
269 et al., 2014) [55]. ECMWF SM was found by Albergel et al. (2012) [56] to represent very well the SM

270 variability at large scales. It is also known to give erroneous values in some areas (Louvet et al., 2015
271 [57]; Kerr et al., 2016 [10]).

272 The NDVI product used in this study was obtained from the 16 day NDVI MODIS Aqua and
273 Terra data, with a 1 km resolution. This product was re-gridded in the EASE 2.0 grid in order to make
274 it comparable with SMOS-IC and SMOSL3 SM. Different studies have shown that τ at microwave
275 frequencies has high spatial correspondences with MODIS NDVI (De Jeu and Owe, 2003 [58]; Andela
276 et al., 2013 [59]) even though both products have shown sensitivity to different aspects of the
277 vegetation dynamics (Grant et al., 2016 [23]).

278 2.4 Inter-comparison

279 The inter-comparison was made for both SMOS-IC and SMOSL3 products by direct comparison
280 between SM (m^3/m^3) and τ , against, respectively, the ECMWF SM and MODIS NDVI products. This
281 section explains the filtering which was applied to the latter datasets and the metrics used in the
282 evaluation process.

283 2.4.1 Data filtering

284 In the evaluation step, only ascending SMOS SM retrievals were selected (Al-Yaari et al., 2014
285 [8][53]). Flags associated with SMOSL3 were used to filter both SMOSL3 and SMOS-IC.

286 For the SMOSL3 SM product, a quality index (DQX) estimates the retrieval quality. In this study, data
287 with $\text{DQX} > 0.06 \text{ m}^3/\text{m}^3$ were excluded. In parallel, the Level 3 RFI probability flag was used to filter
288 out SM data contaminated by RFI. SM retrievals with an associated RFI probability higher than 20%
289 and frozen areas were removed (surface temperature $< 273.15 \text{ K}$). The SMOS-IC and SMOSL3 filtered
290 retrievals of SM and τ used in the study were inter-compared for the same dates. For both SMOS
291 products (SMOSL3 and SMOS-IC), SM values out of the range $0 - 0.6 \text{ m}^3/\text{m}^3$ (Dorigo et al., 2013 [60])
292 and τ values out of the range $0 - 2$ were filtered out. We only considered pixels with temporal series of at
293 least 15 values for the product inter-comparison.

294 In order to compare τ with MODIS NDVI, the daily τ values were re-gridded to 16-day mean
295 values produced every 8 days following the same methodology as described in Grant et al. (2016)
296 [23].

297 2.4.2 Metrics

298 For evaluation purposes, the following metrics were used: Pearson correlation coefficient (R),
299 bias, root mean square difference (RMSD) and unbiased RMSD (ubRMSD). Equations for the
300 calculation of the SM metrics are the following:

$$301 \quad R = \frac{\sum_{i=1}^n (SM_{EC(i)} - \overline{SM_{EC}}) (SM_{SMOS(i)} - \overline{SM_{SMOS}})}{\sqrt{\sum_{i=1}^n (SM_{EC(i)} - \overline{SM_{EC}})^2 \sum_{i=1}^n (SM_{SMOS(i)} - \overline{SM_{SMOS}})^2}}$$

$$302 \quad bias = \overline{(SM_{SMOS} - SM_{EC})}$$

$$303 \quad RMSD = \sqrt{\overline{(SM_{SMOS} - SM_{EC})^2}}$$

$$304 \quad ubRMSD = \sqrt{RMSD^2 - bias^2}$$

305 where n is the number of SM data pairs, SM_{SMOS} is the SMOS SM product (SMOSL3 SM or SMOS-
306 IC) and SM_{EC} is the ECMWF SM. It should be noted the use of RMSD instead of root mean square
307 error (RMSE) as ECMWF SM contain errors and cannot be considered as the "true" ground SM value

308 (Al-Yaari et al., 2014 [53]). In this study, only significant correlations were considered by means of a p-value
 309 filtering for SM retrievals, i.e. pixels where the p-value was above 0.05 were filtered out.

310 In order to evaluate τ , R was calculated as follows:

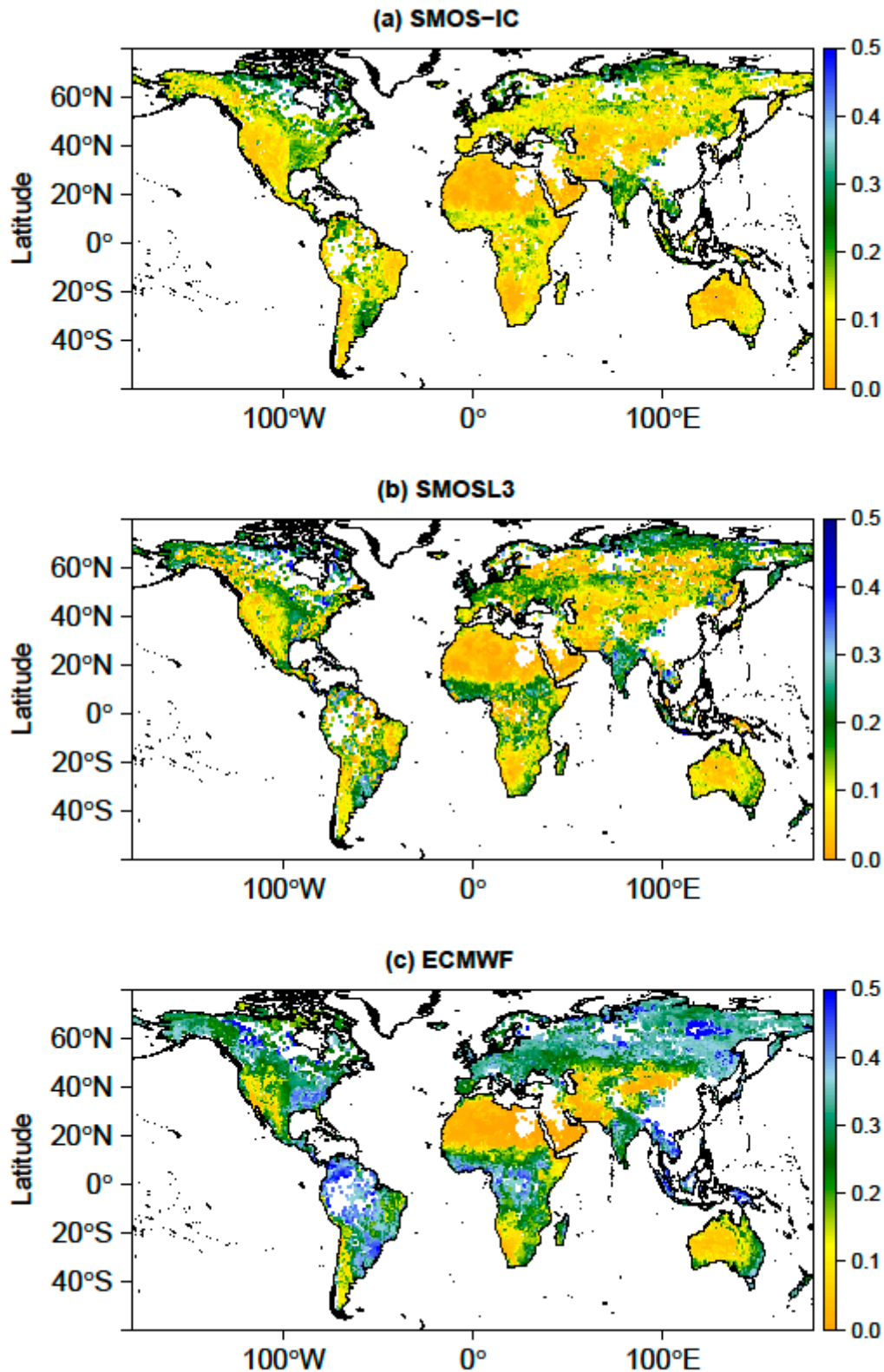
$$311 \quad R = \frac{\sum_{i=1}^n (NDVI_i - \overline{NDVI}) (\tau_{SMOS(i)} - \overline{\tau_{SMOS}})}{\sqrt{\sum_{i=1}^n (NDVI_i - \overline{NDVI})^2 \sum_{i=1}^n (\tau_{SMOS(i)} - \overline{\tau_{SMOS}})^2}}$$

312 where τ_{SMOS} is the vegetation optical depth at nadir (τ) retrieved from the SMOSL3 or SMOS-IC
 313 product.

314 3. Results and discussion

315 3.1 Soil moisture

316 Figure 1 shows the values of the temporal mean SM over the globe and over the period 2010-
 317 2015 for the three SM datasets considered in this study: (a) SMOS-IC, (b) SMOSL3 SM, and (c)
 318 ECMWF. It should be kept in mind that ECMWF SM is representative of the first 0-7 cm of the soil
 319 surface (Albergel et al., 2012 [61]) and the inherent nature of the simulated soil moisture (Koster et
 320 al., 2009 [62]) is different to that measured by the SMOS satellite observations, which are sensitive to
 321 the first ~ 0-3 cm of the soil surface (Escorihuela et al., 2010 [63]; Njoku and Kong et al., 1977 [64]). In
 322 Figure 1, ECMWF SM must be analyzed in terms of spatial patterns rather than absolute values.
 323 Although Figure 1 (a) and (b) have many similarities, some spatial patterns showed by the ECMWF
 324 SM product are in better agreement with SMOS-IC than with SMOS L3 SM. For instance, over the
 325 Appalachian region in the Eastern US, SMOSL3 SM shows a dry area whereas SMOS-IC SM is closer
 326 to ECMWF, as these regions are known to be relatively wetter than the regions of west and midwest
 327 (Sheffied et al., 2004 [65]; Fan et al., 2004 [66]). This was partly explained by differences between
 328 ECOCLIMAP and IGBP and the use of ECMWF SM data in Mahmoodi et al., 2015 [67]. On the other
 329 hand, drier retrievals were found for SMOS-IC in the intertropical regions of Africa, for instance over
 330 the savannas and grasslands of Sahel. Over these regions SMOS-L3 SM is closer to ECMWF SM than
 331 SMOS-IC SM.



332

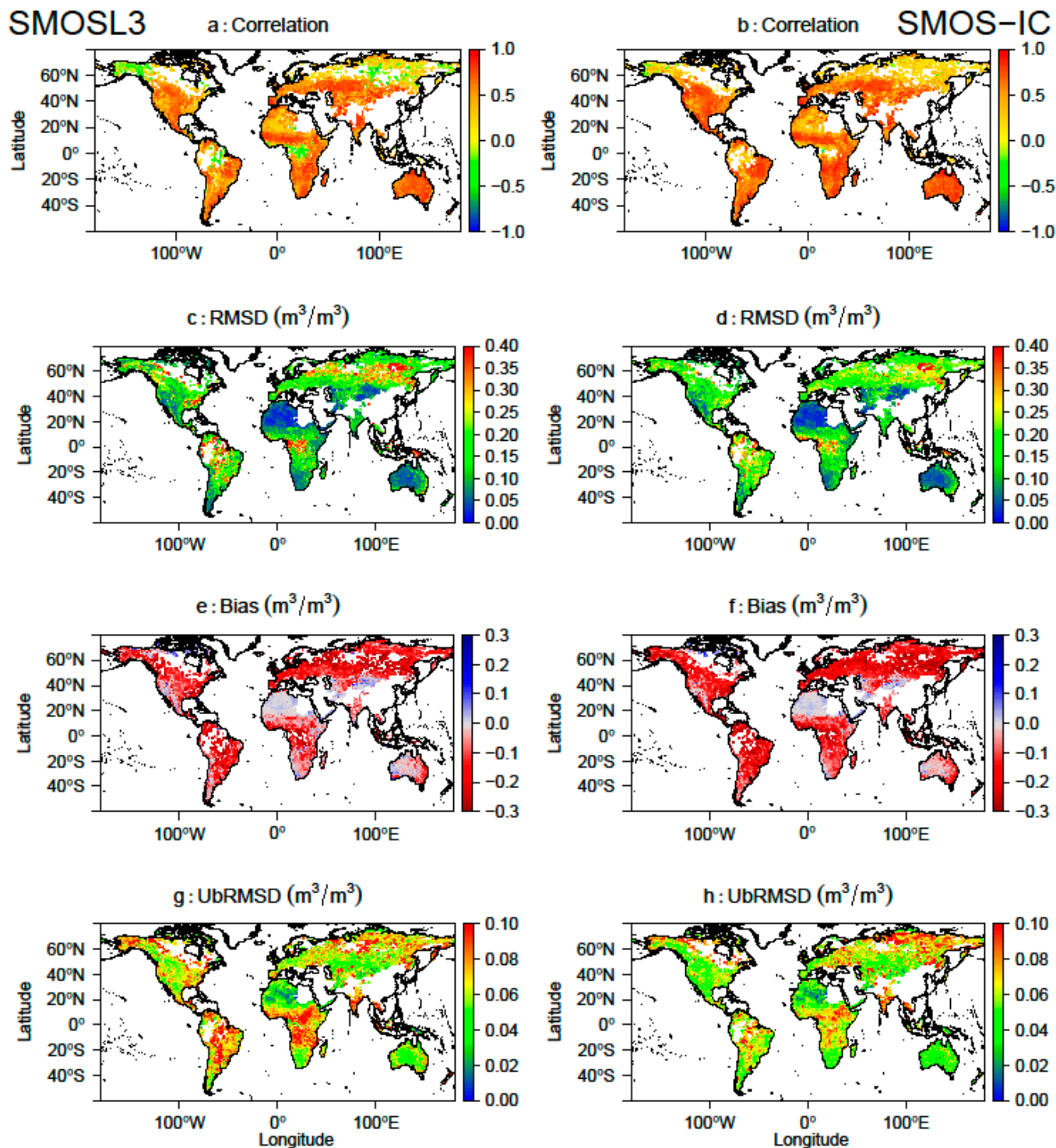
333 Figure 1: Temporal mean of soil moisture (m³/m³) during 2010-2015: (a) SMOS-IC, (b) SMOSL3 SM,
 334 and (c) ECMWF data. White values mean "no valid SMOS data".

335 Figure 2 displays different time series metrics derived from the direct comparison between
 336 SMOSL3 SM (a) and SMOS-IC SM (b) with ECMWF SM for 2010-2015. According to correlation (R)
 337 results, lowest R values were found in forests for both products. A lower number of negative R values

338 were found between the SMOS-IC and ECMWF SM products. Conversely, SMOSL3 SM yielded
339 negative correlations with ECMWF SM over several forest regions, namely the boreal forests of
340 Alaska, Canada and Russia, and the tropical forests of Amazon and Congo basins. Over the non-
341 forested biomes, R values were also found to be generally higher for SMOS-IC, when compared to
342 SMOSL3 SM. Substantial differences were found in terms of RMSD and ubRMSD: in general, lower
343 values were obtained for the SMOS-IC product, especially over the intertropical regions of America
344 and Africa (in terms of ubRMSD) and the boreal forests of Eurasia (in terms of RMSD). On the other
345 hand, results do not show important differences in terms of bias between the two SMOS products:
346 both SMOS-IC and SMOSL3 SM products are generally much drier than ECMWF SM, except over
347 some arid and semi-arid areas (deserts in central Asia and Australia, Sahara in Northern Africa). The
348 general negative values of the bias can be partly explained by the differences in sampling depths
349 between the SMOS observations (~ 0-3 cm top soil layer) and the modeled ECMWF SM (0-7 cm top
350 soil layer). Considering this difference in sampling depths, the observed difference in SM bias
351 patterns in Figure 2, should be interpreted with care.

352

353



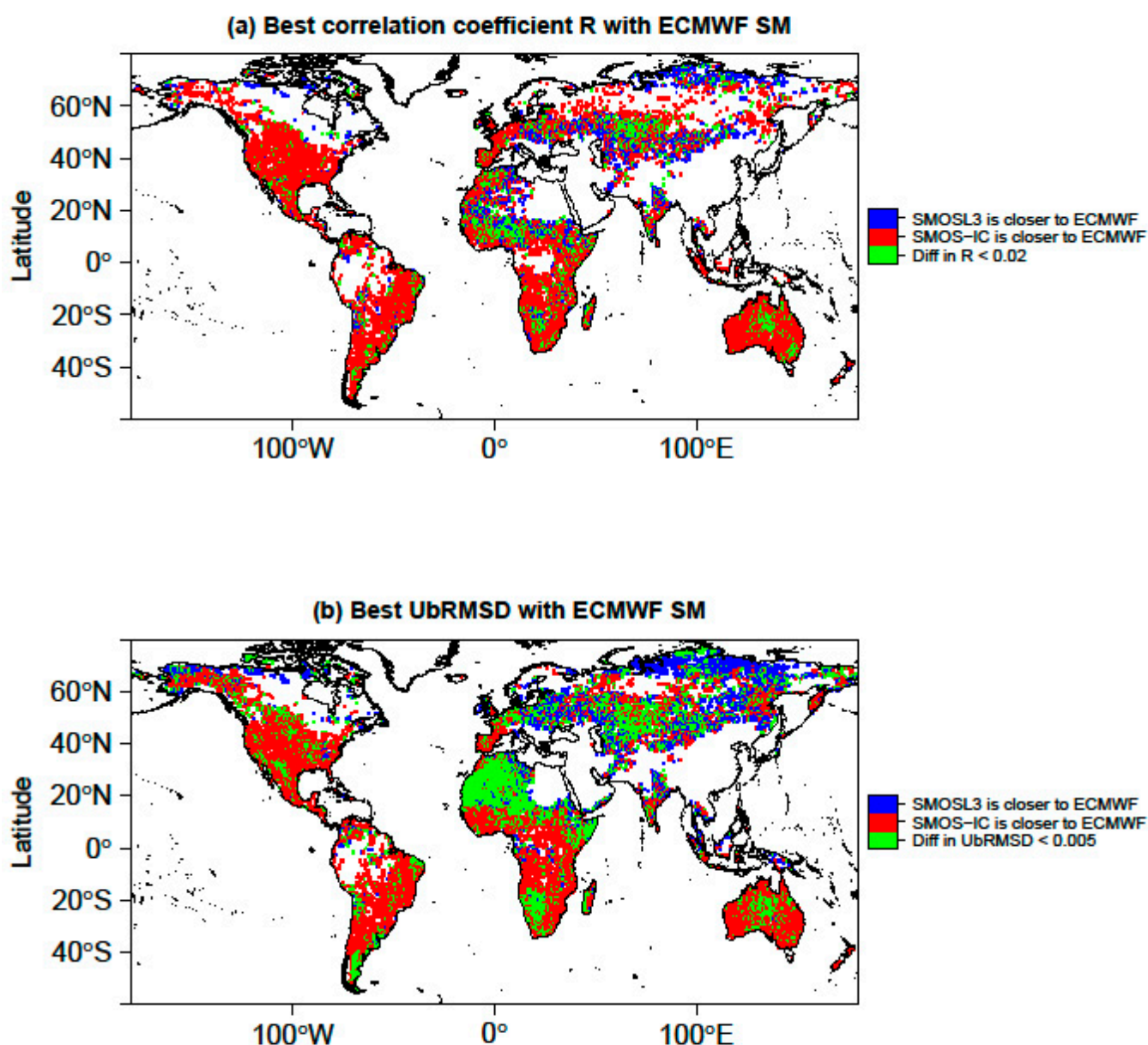
354

355

356 Figure 2: Pixel-based statistics during 2010-2015 computed between ECMWF SM simulations and
 357 SMOSL3 SM (left) and SMOS-IC (right) SM retrievals: (a)(b) correlation coefficient, (c)(d) RMSD, (e)(f)
 358 bias, and (g)(h) ubRMSD.

359

360 Figure 3 is focused on the results in terms of correlation and ubRMSD, considered as first order
 361 criteria. It displays a world map which shows where the best correlation coefficient (R) and ubRMSD
 362 are obtained by comparing ECMWF SM with SMOS-IC SM (red) or SMOSL3 SM (blue) in the period
 363 2010-2015. Areas where the result differs by less than 0.02 in terms of R values between SMOSL3 SM
 364 and SMOS-IC are represented in green color. This threshold is different for the ubRMSD metric and
 365 it was set to $0.005 \text{ m}^3/\text{m}^3$. It can be seen that the red color is dominant, meaning that SMOS-IC SM is
 366 generally closer to ECMWF in terms of temporal dynamics. There are some exceptions. For instance,
 367 regions colored in blue (SMOSL3 is closer to ECMWF than SMOS-IC) can be found especially for the
 368 ubRMSD metric, in central Europe, central and Northern Asia. It should be noted here that only pixels
 369 with significant correlations i.e. $p\text{-value} < 0.05$ and a number of data (>15) are presented.

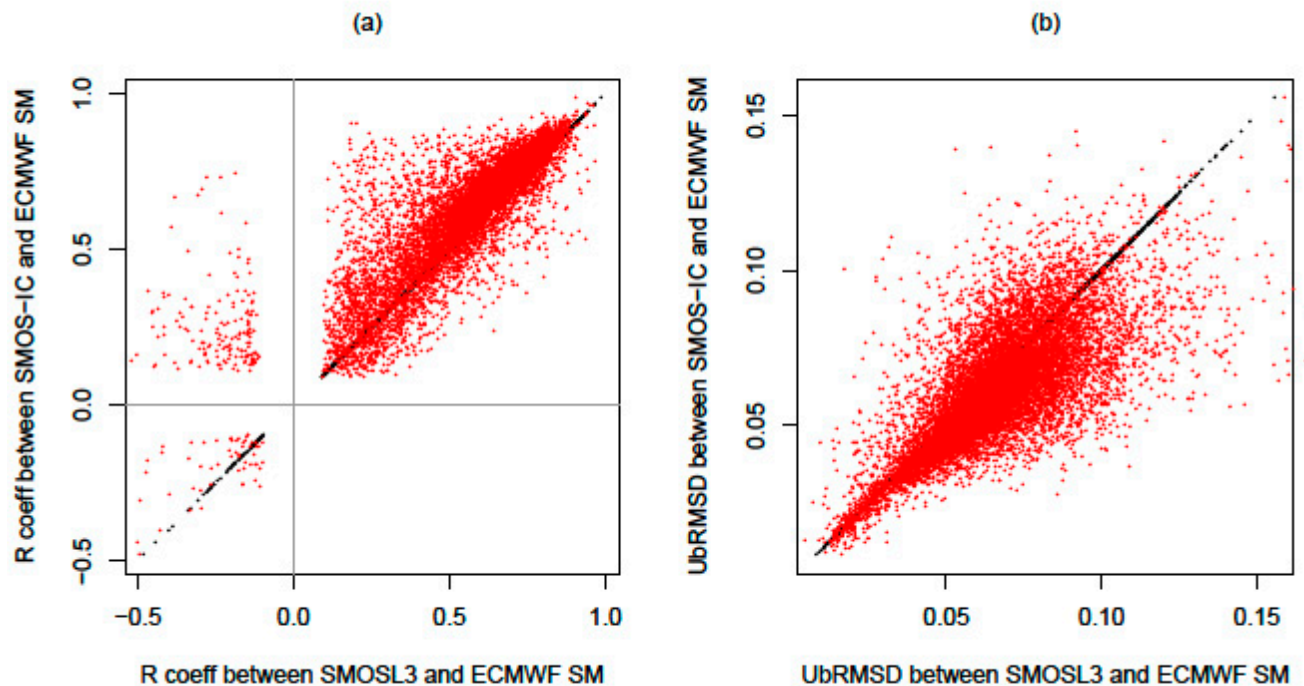


370

371

372 Figure 3: Comparison of the SMOS SM products with respect to ECMWF showing: (a) where SMOS-
 373 IC SM (red) or SMOSL3 SM (blue) leads to the best correlation coefficient, or where the difference in
 374 R < 0.02 (green) among both SMOS products; (b) where SMOS-IC SM (red) or SMOSL3 SM (blue) lead
 375 to the lowest ubRMSE or where the difference in ubRMSD < 0.005 (green).

376 In order to better assess the range of R and ubRMSD values, the dispersion diagrams displayed
 377 in Figure 4 show the scatter plot of both metrics for all pixels and for both SMOS products (SMOS-IC
 378 and SMOSL3 SM). In terms of correlation, the R values are generally larger for SMOS-IC. There are
 379 also a number of pixels where SMOSL3 SM yields negative correlations whereas R is positive for
 380 SMOS-IC. In terms of ubRMSD, the largest number of pixels with lower ubRMSD corresponds to the
 381 SMOS-IC SM product.



382

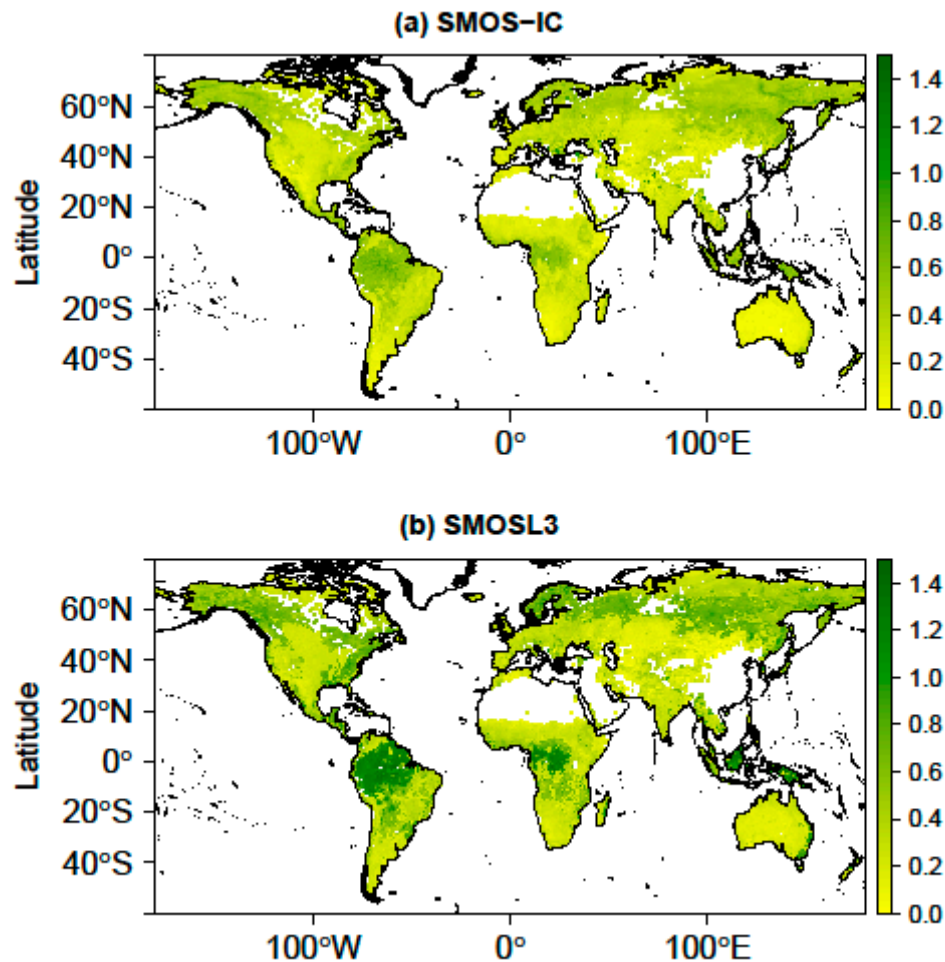
383

384 Figure 4: Scatter plot of correlation (a) and ubRMSD values (b) obtained by comparing both SMOS-
 385 IC and SMOSL3 SM to ECMWF SM.

386 3.2 Vegetation optical depth

387 The evaluation of the accuracy of the τ values retrieved from SMOS at global scale is not a simple
 388 issue due to the absence of a consensus on the reference values to be considered at large scale coming
 389 from models or in situ measurements. Some studies have been done at local scale. For instance, over
 390 croplands and grasslands, τ values at L-band vary generally between 0 and 0.6 (Saleh et al., 2006 [68],
 391 Wigneron et al., 2007 [11]). Over forests and from L-band radiometer measurements, Ferrazzoli et al.
 392 (2002) [69] found maximum values of $\tau \sim 0.9$, and Grant et al. (2008) [70] found values of $\tau \sim 0.6-0.7$
 393 for a mature pine forest stand in *les Landes* forest, and $\tau \sim 1$ for a mature deciduous (beech) canopy in
 394 Switzerland.

395 Figure 5 shows a global map of the temporal mean of the retrieved τ values for both SMOS-IC
 396 and SMOSL3 products. Both products show τ values which are sensitive to vegetation, as the highest
 397 τ values were found for the main boreal and tropical forests. It must be noted that the τ values coming
 398 from the SMOSL3 product were larger than those obtained by the SMOS-IC product.

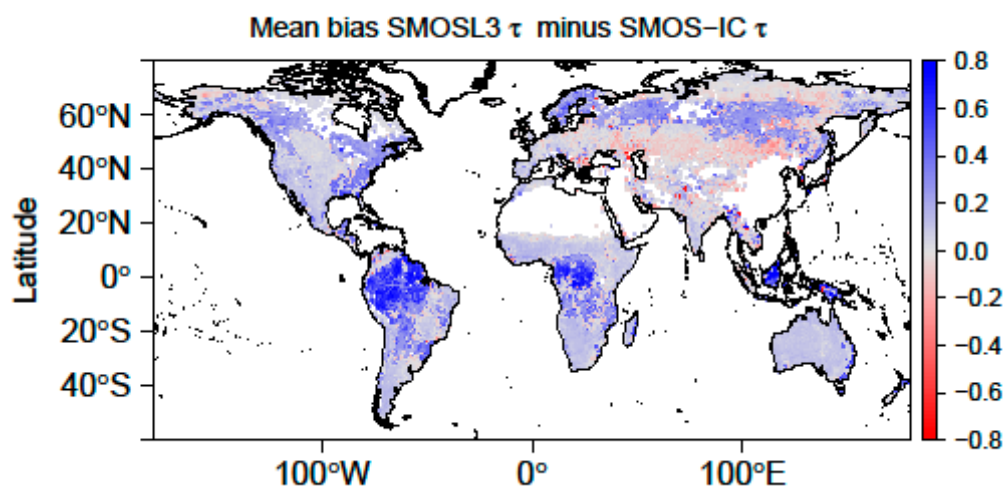


399

400

Figure 5: Temporal mean of τ during 2010-2015: (a) SMOS-IC and (b) SMOSL3.

401 In order to identify possible patterns, Figure 6 shows a global map which illustrates the
 402 differences of τ between both SMOS datasets (SMOSL3 minus SMOS-IC). This result shows that the
 403 greatest differences between both τ datasets were found over forest areas, particularly tropical
 404 regions; namely Amazon and Congo River basins and Borneo and New Guinea tropical forests,
 405 where significantly larger τ values were obtained with SMOSL3.



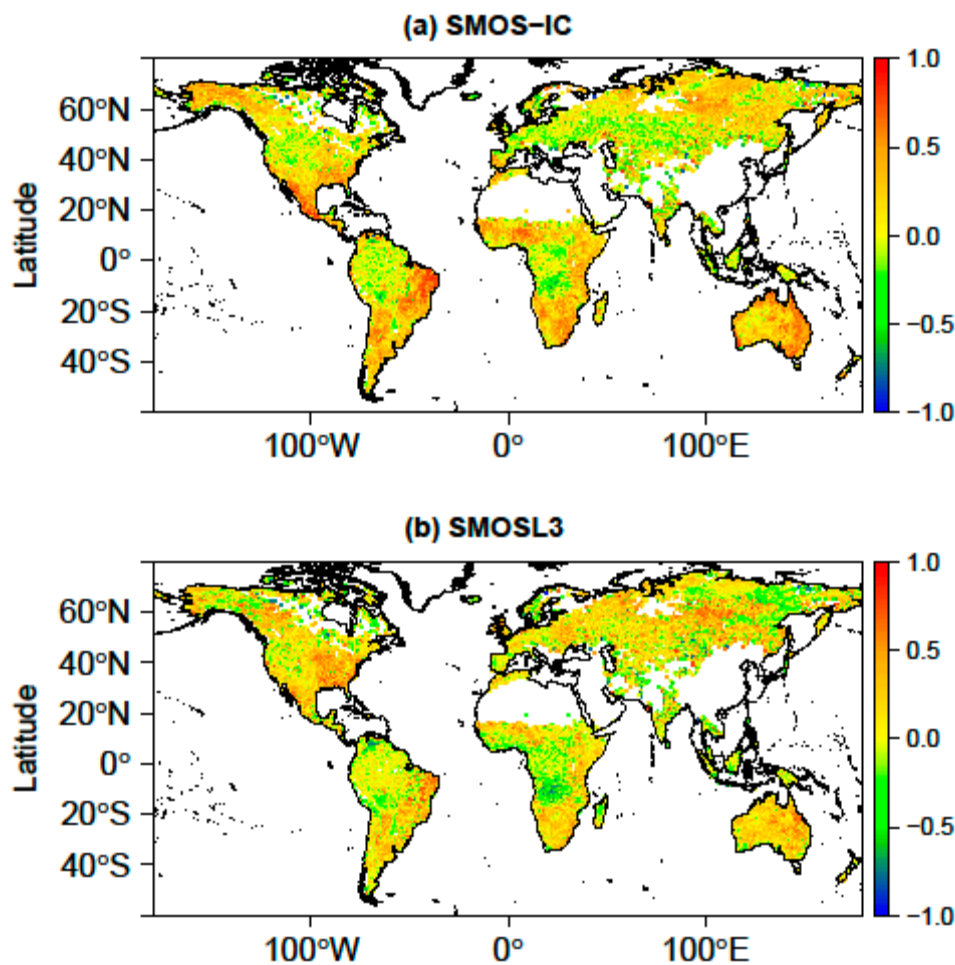
406

407

Figure 6: mean bias: SMOSL3 τ minus SMOS-IC τ for 2010-2015.

408

409 Figure 7 shows the correlations obtained by comparing the SMOS-IC and SMOSL3 τ datasets
 410 to MODIS NDVI. All correlations values are presented here including those not significant as done
 411 by Grant et al. (2016) [23]. It can be noted that slightly higher correlation values are generally obtained
 412 with SMOS-IC especially in the west of Mexico, the Northeastern regions of Brazil and some parts of
 413 the Sahel. Conversely higher R values were obtained in western and central Europe with SMOSL3.
 414 The lowest correlations were found generally over forests for both SMOS products; a result which
 415 can be partly related to the tendency of NDVI to saturate for high biomass and LAI values. However,
 416 higher R values were obtained with SMOS-IC for some areas of the boreal forests and the tropical
 forests of Africa.



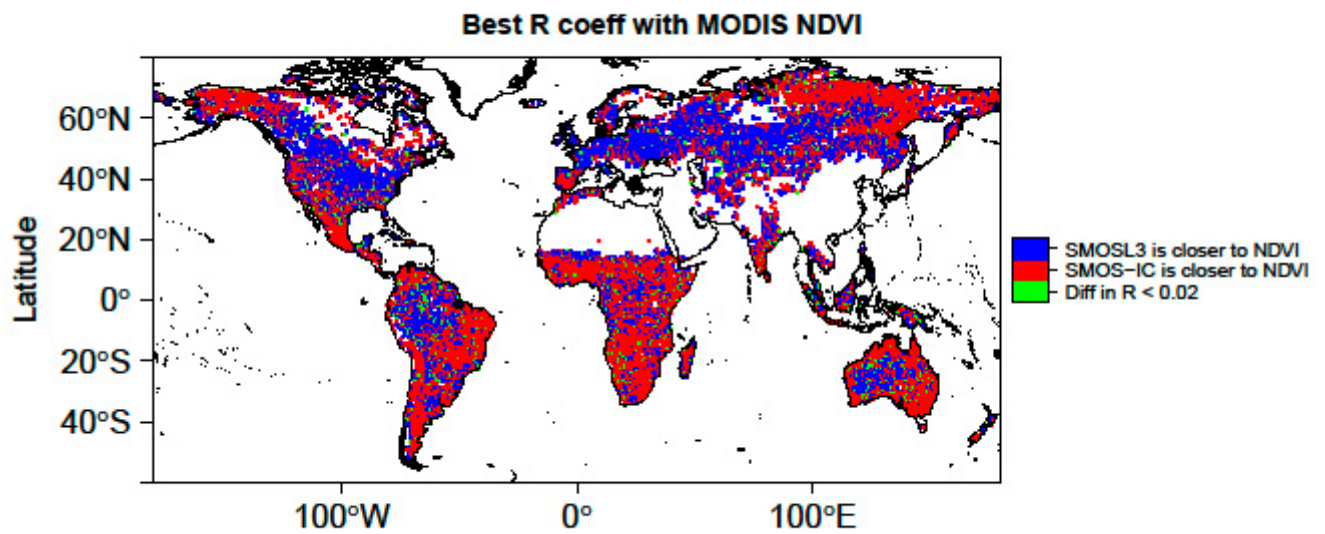
417

418

419 Figure 7: Correlation (R) values obtained between SMOS-IC τ and MODIS NDVI (a) and between
 SMOSL3 τ and MODIS NDVI (b).

420

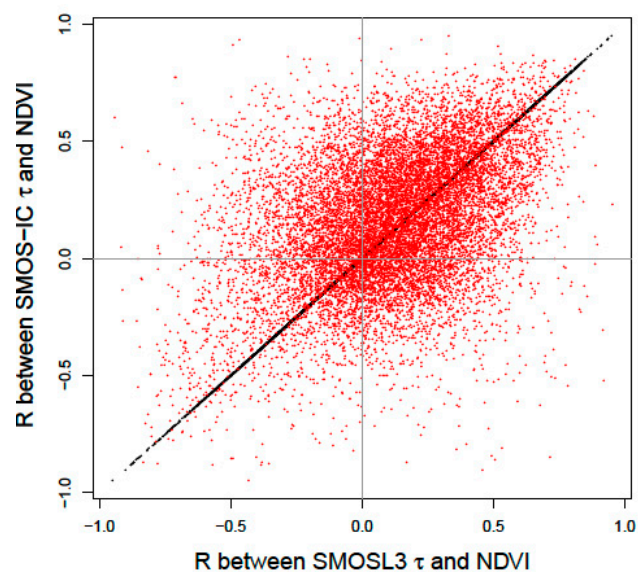
421 A global map that shows for each pixel which τ dataset (SMOSL3 or SMOS-IC) leads to the
 422 largest correlation (R) values with MODIS NDVI is presented in Figure 8. Over northern mid-latitudes,
 423 larger correlations were generally obtained with SMOSL3. However, except for these regions, the
 424 highest R values were generally obtained with SMOS-IC while no clear patterns were found in terms
 425 of longitude. Figure 9 shows a dispersion diagram in order to assess the range of correlation values
 426 found for both SMOS τ datasets against MODIS τ . The diagram generally yields positive correlations,
 although a non-negligible number of negative correlations can be noted for both SMOS products.



427

428

429 Figure 8: Comparison of SMOS-IC and SMOS-L3 τ products with respect to MODIS NDVI: higher
 430 correlation (R) values between SMOS-IC τ and MODIS NDVI (red) or between SMOSL3 τ and MODIS
 431 NDVI (blue) and where the difference in R < 0.02 (green).



432

433 Figure 9: Scatter plot showing correlation values obtained between SMOS-IC τ and MODIS NDVI
 434 against correlation values obtained between the τ from SMOSL3 and MODIS NDVI.

435

436 4. Summary and conclusions

437 This study presents an alternative SMOS SM and τ product, referred to as SMOS-IC. In terms of
 438 soil moisture, the presentation is based on an inter-comparison between SMOS-IC, the official Level

3 SMOS SM product (SMOSL3, V300), and a modeled SM product (ECMWF SM). The SMOS-IC product is based on the retrieval of SM and τ over pixels treated as homogeneous by means of the L-MEB model inversion. SMOS-IC uses the multi-angular and dual-polarization SMOSL3 TB product as the main input for the L-MEB model inversion. The L-MEB model input parameters (effective vegetation scattering albedo ω and the roughness parameter H_R) are estimated as a function of IGBP land category classes which compose the pixel. These parameter values are derived from previous analyses made by Fernandez-Moran et al. (2016) [31] and global maps of the roughness H_R parameter estimated by Parrens et al. (2016) [30]. Conversely, the SMOSL3 product considers different fractions over the pixel and performs SM and τ retrievals over the main fraction of the pixel (usually low vegetation) or over forests in some cases. In the SMOSL3 retrieval algorithm, the TB value of the pixel fraction which is not considered in the retrieval (the forest fraction in general) is estimated based on auxiliary ECMWF SM data. This specific approach may lead to dry SM bias in forested regions, as noted by Wigneron et al. (2012) [28]. Currently, in the SMOSL3 V300 retrieval algorithm, the values of the vegetation and soil roughness parameters differ mainly between forest and low vegetation categories.

The SMOSL3 and SMOS-IC soil moisture retrievals were compared globally against ECMWF SM data for the period 2010-2015. This evaluation extends the work of Fernandez-Moran et al. (2016) [31] who evaluated a preliminary version of the SMOS-IC product at local scale using numerous in situ SM stations from ISMN and found higher R and lower ubRMSE with SMOS-IC than with the SMOSL3 V300 product. At global scale, both the SMOS-IC and SMOSL3 SM products were generally found to be drier than the ECMWF SM product. However, the larger soil sampling depth of the ECMWF SM (0-7 cm) with respect to SMOS SM (~ 0 - 3 cm), as well as the inherently different nature of simulated soil moisture (Koster et al., 2009 [62]), makes it difficult to truly assess the performance of the SMOS products in terms of bias at global scale. In terms of temporal variations, higher correlation values and lower ubRMSD values were generally found between SMOS-IC SM and ECMWF SM, than between SMOSL3 SM and ECMWF SM.

The ECMWF SM data set used in this study is not "truth", and a larger inter-comparison of SMOS-IC and SMOSL3 against other modeled SM products should be made in the future to confirm the very preliminary results found in this study. In terms of τ values, the SMOS-IC and SMOSL3 τ products were compared to MODIS NDVI values over 2010-2015 in terms of correlation values. The SMOS-IC τ product presents a lower range of values (~ 0-0.6) than the one obtained with the SMOSL3 τ product (~ 0-1.2). The latter range of τ values (obtained for SMOSL3) is in better agreement than SMOS-IC τ , with the ranges of retrieved τ values based on in situ L-band radiometric measurements (τ ~0.6 -1.0) performed over mature coniferous and deciduous forests in Europe. Conversely, slightly higher correlation values were obtained between SMOS-IC τ and MODIS NDVI, than between SMOSL3 τ and MODIS NDVI, except in the Amazon basin and in regions of the northern mid-latitudes.

The τ results should also be interpreted with care: the NDVI index is derived from optical sensors while the τ index is derived from L-band microwave measurements and therefore can sense deeper through the vegetation canopy. Moreover, the NDVI index is used to monitor the green vegetation, while the τ index is related to the whole vegetation water content (including stems, trunks, branches and senescent vegetation elements). So at L-band, the NDVI index (as the LAI index) is only a proxy which is used to provide an estimate of τ over rather low vegetation covers during the vegetation growth (O'Neill et al, 2012 [35]; Wigneron et al., 2007 [11]; Lawrence et al., 2014 [71]; Grant et al., 2016 [23]). A larger inter-comparison of the SMOS-IC and SMOSL3 τ products against different vegetation data sets (remotely sensed products, LAI, forest biomass) should be made in the future to confirm the results found in this study.

As for the Level 2 and 3 algorithms, based on rather complex and detailed concepts and auxiliary data sets, the simple SMOS-IC algorithm will be improved regularly and will be used to improve L2 and L3 SMOS retrieval algorithms. These different approaches are complementary and a regular inter-comparison analysis between them should be of great benefit to improve the L-MEB inversion, and ultimately the SM and τ products retrieved from the SMOS observations.

491 **Acknowledgements**

492 The authors would like to thank the TOSCA (Terre Océan Surfaces Continentales et
493 Atmosphère) CNES program and the European Space Agency (ESA) for funding this study. The
494 authors acknowledge CATDS for the SMOSL3 dataset (<http://catds.ifremer.fr>) and the cooperation of
495 the different soil moisture in situ networks of the International Soil Moisture Network (ISMN) project.

496 **Author contributions**

497 Jean-Pierre Wigneron and Roberto Fernandez-Moran designed the SMOS-IC product with the
498 helpful contribution of CESBIO. Arnaud Mialon and Ali Mahmoodi optimized the code, improved
499 the data format and processed the data set at CESBIO. Amen Al-Yaari made the analysis of the IC
500 data and produced all the figures; Yann Kerr, Gabrielle de Lannoy, Ahmad Al Bitar and Ernesto
501 Lopez-Baeza provided scientific expertise; Roberto Fernandez-Moran and Jean-Pierre Wigneron
502 wrote the paper.

503 **Conflicts of interest**

504 The authors declare no conflicts of interest.

505 **References**

- 506 1. Kerr, Y. H.; Waldteufel, P.; Richaume, P.; Wigneron, J. P.; Ferrazzoli, P.; Mahmoodi, A.;
507 Bitar, A. Al; Cabot, F.; Gruhier, C.; Juglea, S. E.; Leroux, D.; Mialon, A.; Delwart, S. The SMOS
508 Soil Moisture Retrieval Algorithm. *Geosci. Remote Sens.* **2012**, *50*, 1384–1403.
- 509 2. Entekhabi, D.; Njoku, E. G.; O'Neill, P. E.; Kellogg, K. H.; Crow, W. T.; Edelstein, W.
510 N.; Entin, J. K.; Goodman, S. D.; Jackson, T. J.; Johnson, J.; Kimball, J.; Piepmeier, J. R.; Koster, R.
511 D.; Martin, N.; McDonald, K. C.; Moghaddam, M.; Moran, S.; Reichle, R.; Shi, J. C.; Spencer, M.
512 W.; Thurman, S. W.; Tsang, L.; Van Zyl, J. The soil moisture active passive (SMAP) mission. *Proc.*
513 *IEEE* **2010**, *98*, 704–716.
- 514 3. Brocca, L.; Melone, F.; Moramarco, T.; Wagner, W.; Naeimi, V.; Bartalis, Z.; Hasenauer,
515 S. Improving runoff prediction through the assimilation of the ASCAT soil moisture product. *Hydrol.*
516 *Earth Syst. Sci.* **2010**, *14*, 1881–1893.
- 517 4. Hollmann, R.; Merchant, C. J.; Saunders, R.; Downy, C.; Buchwitz, M.; Cazenave, A.;
518 Chuvieco, E.; Defourny, P.; De Leeuw, G.; Forsberg, R.; Holzer-Popp, T.; Paul, F.; Sandven, S.;
519 Sathyendranath, S.; Van Roozendaal, M.; Wagner, W. The ESA climate change initiative: Satellite
520 data records for essential climate variables. *Bull. Am. Meteorol. Soc.* **2013**, *94*, 1541–1552.
- 521 5. Al Bitar, A.; Mialon, A.; Kerr, Y.; Cabot, F.; Richaume, P.; Jacqueline, E.; Quesney, A.;
522 Mahmoodi, A.; Tarot, S.; Parrens, M.; Al-yaari, A.; Pellarin, T.; Rodriguez-Fernandez, N.; Wigneron,
523 J.-P. The Global SMOS Level 3 daily soil moisture and brightness temperature maps. *Earth Syst. Sci.*
524 *Data Discuss.* **2017**, 1–41.
- 525 6. Kerr, Y. H.; Waldteufel, P.; Wigneron, J. P.; Martinuzzi, J. M.; Font, J.; Berger, M. Soil
526 moisture retrieval from space: The Soil Moisture and Ocean Salinity (SMOS) mission. *IEEE Trans.*
527 *Geosci. Remote Sens.* **2001**, *39*, 1729–1735.
- 528 7. Mialon, A.; Richaume, P.; Leroux, D.; Bircher, S.; Bitar, A. Al; Pellarin, T.; Wigneron, J.
529 P.; Kerr, Y. H. Comparison of Dobson and Mironov dielectric models in the SMOS soil moisture
530 retrieval algorithm. *IEEE Trans. Geosci. Remote Sens.* **2015**, *53*, 3084–3094.
- 531 8. Al-Yaari, A.; Wigneron, J. P.; Ducharne, A.; Kerr, Y. H.; Wagner, W.; De Lannoy, G.;
532 Reichle, R.; Al Bitar, A.; Dorigo, W.; Richaume, P.; Mialon, A. Global-scale comparison of passive
533 (SMOS) and active (ASCAT) satellite based microwave soil moisture retrievals with soil moisture
534 simulations (MERRA-Land). *Remote Sens. Environ.* **2014**, *152*, 614–626.
- 535 9. Al-Yaari, A.; Wigneron, J. P.; Ducharne, A.; Kerr, Y.; Fernandez-Moran, R.; Parrens, M.;
536 Bi-tar, A. Al; Mialon, A.; Richaume, P. Evaluation of the most recent reprocessed SMOS soil
537 moisture products: Comparison between SMOS level 3 V246 and V272. In *IEEE International*
538 *Geoscience and Remote Sensing Symposium (IGARSS)*; IEEE: Milan (Italy), 2015; pp. 2493–2496.

- 539 10. Kerr, Y. H.; Al-Yaari, A.; Rodriguez-Fernandez, N.; Parrens, M.; Molero, B.; Leroux, D.;
540 Bircher, S.; Mahmoodi, A.; Mialon, A.; Richaume, P.; Delwart, S.; Al Bitar, A.; Pellarin, T.; Bindlish,
541 R.; Jackson, T. J.; Rüdiger, C.; Waldteufel, P.; Mecklenburg, S.; Wigneron, J.-P. Overview of SMOS
542 performance in terms of global soil moisture monitoring after six years in operation. *Remote Sens.*
543 *Environ.* **2016**, *180*, 40–63.
- 544 11. Wigneron, J. P.; Kerr, Y.; Waldteufel, P.; Saleh, K.; Escorihuela, M. J.; Richaume, P.;
545 Ferrazzoli, P.; de Rosnay, P.; Gurney, R.; Calvet, J. C.; Grant, J. P.; Guglielmetti, M.; Hornbuckle,
546 B.; Mätzler, C.; Pellarin, T.; Schwank, M. L-band Microwave Emission of the Biosphere (L-MEB)
547 Model: Description and calibration against experimental data sets over crop fields. *Remote Sens.*
548 *Environ.* **2007**, *107*, 639–655.
- 549 12. Rahmoune, R.; Ferrazzoli, P.; Kerr, Y. H.; Richaume, P. SMOS level 2 retrieval algorithm
550 over forests: Description and generation of global maps. *IEEE J. Sel. Top. Appl. Earth Obs. Remote*
551 *Sens.* **2013**, *6*, 1430–1439.
- 552 13. Rahmoune, R.; Ferrazzoli, P.; Singh, Y. K.; Kerr, Y. H.; Richaume, P.; Al Bitar, A. SMOS
553 retrieval results over forests: Comparisons with independent measurements. *IEEE J. Sel. Top. Appl.*
554 *Earth Obs. Remote Sens.* **2014**, *7*, 3858–3866.
- 555 14. Schwank, M.; Mätzler, C.; Guglielmetti, M.; Flühler, H. L-band radiometer
556 measurements of soil water under growing clover grass. *IEEE Trans. Geosci. Remote Sens.* **2005**, *43*,
557 2225–2236.
- 558 15. Schwank, M.; Wigneron, J. P.; López-Baeza, E.; Völksch, I.; Mätzler, C.; Kerr, Y. H. L-
559 band radiative properties of vine vegetation at the MELBEX III SMOS cal/val site. *IEEE Trans.*
560 *Geosci. Remote Sens.* **2012**, *50*, 1587–1601.
- 561 16. Jackson, T. J.; Schmugge, T. J. Vegetation effects on the microwave emission of soils.
562 *Remote Sens. Environ.* **1991**, *36*, 203–212.
- 563 17. Mo, T.; Choudhury, B. J.; Schmugge, T. J.; Wang, J. R.; Jackson, T. J. A model for
564 microwave emission from vegetation-covered fields. *J. Geophys. Res.* **1982**, *87*, 11229.
- 565 18. Wigneron, J. P.; Chanzy, A.; Calvet, J. C.; Bruguier, N. A simple algorithm to retrieve
566 soil moisture and vegetation biomass using passive microwave measurements over crop fields.
567 *Remote Sens. Environ.* **1995**, *51*, 331–341.
- 568 19. Grant, J. P.; Wigneron, J. P.; Drusch, M.; Williams, M.; Law, B. E.; Novello, N.; Kerr,
569 Y. Investigating temporal variations in vegetation water content derived from SMOS optical depth.
570 In *International Geoscience and Remote Sensing Symposium (IGARSS)*; 2012; pp. 3331–3334.
- 571 20. Schneebeli, M.; Wolf, S.; Kunert, N.; Eugster, W.; Mätzler, C. Relating the X-band
572 opacity of a tropical tree canopy to sapflow, rain interception and dew formation. *Remote Sens.*

573 *Environ.* **2011**, *115*, 2116–2125.

574 21. Guglielmetti, M.; Schwank, M.; Mätzler, C.; Oberdörster, C.; Vanderborght, J.; Flübler,
575 H. FOSMEX: Forest soil moisture experiments with microwave radiometry. *IEEE Trans. Geosci.*
576 *Remote Sens.* **2008**, *46*, 727–735.

577 22. Patton, J.; Member, S.; Hornbuckle, B. Initial Validation of Smos Vegetation Optical
578 Thickness in Iowa. **2012**, *10*, 3791–3794.

579 23. Grant, J. P.; Wigneron, J. P.; De Jeu, R. A. M.; Lawrence, H.; Mialon, A.; Richaume, P.;
580 Al Bitar, A.; Drusch, M.; van Marle, M. J. E.; Kerr, Y. Comparison of SMOS and AMSR-E vegetation
581 optical depth to four MODIS-based vegetation indices. *Remote Sens. Environ.* **2016**, *172*, 87–100.

582 24. Fernandez-Moran, R.; Wigneron, J.-P.; Lopez-Baeza, E.; Al-Yaari, A.; Bircher, S.; Coll-
583 Pajaron, A.; Mahmoodi, A.; Parrens, M.; Richaume, P.; Kerr, Y. Analyzing the impact of using the
584 SRP (Simplified roughness parameterization) method on soil moisture retrieval over different regions
585 of the globe. *Int. Geosci. Remote Sens. Symp.* **2015**, *2015–Novem*, 5182–5185.

586 25. Parrens, M.; Wigneron, J.-P.; Richaume, P.; Al Bitar, A.; Mialon, A.; Fernandez-Moran,
587 R.; Al-Yaari, A.; O'Neill, P.; Kerr, Y. Considering combined or separated roughness and vegetation
588 effects in soil moisture retrievals. *Int. J. Appl. Earth Obs. Geoinf.* **2017**, *55*, 73–86.

589 26. Wigneron, J. P.; Chanzy, A.; Kerr, Y. H.; Lawrence, H.; Shi, J.; Escorihuela, M. J.;
590 Mironov, V.; Mialon, A.; Demontoux, F.; De Rosnay, P.; Saleh-Contell, K. Evaluating an improved
591 parameterization of the soil emission in L-MEB. *IEEE Trans. Geosci. Remote Sens.* **2011**, *49*, 1177–
592 1189.

593 27. Wigneron, J.-P.; Jackson, T. J.; O'Neill, P.; De Lannoy, G.; Rosnay, P. de; Walker, J. P.;
594 Ferrazzoli, P.; Mironov, V.; Bircher, S.; Grant, J. P.; Kurum, M.; Schwank, M.; Munoz-Sabater, J.;
595 N. Das, A. R.; Al-Yaari, A.; Bitar, A. Al; Fernandez-Moran, R.; Lawrence, H.; Mialon, A.; Parrens,
596 M.; Richaume, P.; Rodriguez-Fernandez, N.; Delwart, S.; Kerr., Y. Modelling the passive microwave
597 signature from land surfaces: a review of recent results and application to the L-band SMOS & SMAP
598 soil moisture retrieval algorithms. *Remote Sens. Environ. In press.*

599 28. Wigneron, J. P.; Schwank, M.; Baeza, E. L.; Kerr, Y.; Novello, N.; Millan, C.; Moisy, C.;
600 Richaume, P.; Mialon, A.; Al Bitar, A.; Cabot, F.; Lawrence, H.; Guyon, D.; Calvet, J. C.; Grant, J.
601 P.; Casal, T.; de Rosnay, P.; Saleh, K.; Mahmoodi, A.; Delwart, S.; Mecklenburg, S. First evaluation
602 of the simultaneous SMOS and ELBARA-II observations in the Mediterranean region. *Remote Sens.*
603 *Environ.* **2012**, *124*, 26–37.

604 29. Fernandez-Moran, R.; Wigneron, J.-P.; De Lannoy, G.; Lopez-Baeza, E.; Mialon, A.;
605 Mahmoodi, A.; Parrens, M.; Al Bitar, A.; Richaume, P.; Kerr, Y. Calibrating the effective scattering
606 albedo in the SMOS algorithm: Some first results. In *2016 IEEE International Geoscience and*
607 *Remote Sensing Symposium (IGARSS)*; IEEE, 2016; pp. 826–829.

- 608 30. Parrens, M.; Wigneron, J. P.; Richaume, P.; Mialon, A.; Al Bitar, A.; Fernandez-Moran,
609 R.; Al-Yaari, A.; Kerr, Y. H. Global-scale surface roughness effects at L-band as estimated from
610 SMOS observations. *Remote Sens. Environ.* **2016**, *181*, 122–136.
- 611 31. Fernandez-Moran, R.; Wigneron, J.-P.; De Lannoy, G.; Lopez-Baeza, E.; Mialon, A.;
612 Mahmoodi, A.; Parrens, M.; Al Bitar, A.; Richaume, P.; Kerr, Y. Calibrating the effective scattering
613 albedo in the SMOS algorithm: Some first results. In *IEEE International Geoscience and Remote*
614 *Sensing Symposium (IGARSS)*; IEEE: Beijing (China), 2016; pp. 826–829.
- 615 32. Kaufman, Y. J.; Justice, C. O.; Flynn, L. P.; Kendall, J. D.; Prins, E. M.; Giglio, L.; Ward,
616 D. E.; Menzel, W. P.; Setzer, A. W. Potential global fire monitoring from EOS-MODIS. *J. Geophys.*
617 *Res.* **1998**, *103*, 32215–32238.
- 618 33. Rouse, J. W.; Haas, R. H.; Schell, J. A. Monitoring the vernal advancement and
619 retrogradation (greenwave effect) of natural vegetation. *NASA Goddard Sp. Flight Cent.* 1974, 1–8.
- 620 34. Qi, J.; Chehbouni, A.; Huete, A. R.; Kerr, Y. H.; Sorooshian, S. A modified soil adjusted
621 vegetation index. *Remote Sens. Environ.* **1994**, *48*, 119–126.
- 622 35. O'Neill, P.; Chan, S.; Njoku, E.; Jackson, T.; Bindlish, R. *Soil Moisture Active Passive*
623 *(SMAP) Algorithm Theoretical Basis Document (ATBD). SMAP Level 2 & 3 Soil Moisture*
624 *(Passive), (L2_SM_P, L3_SM_P)*; 2012.
- 625 36. Corbella, I.; Torres, F.; Duffo, N.; González-Gambau, V.; Pablos, M.; Duran, I.; Martín-
626 Neira, M. MIRAS calibration and performance: Results from the SMOS in-orbit commissioning
627 phase. In *IEEE Transactions on Geoscience and Remote Sensing*; 2011; Vol. 49, pp. 3147–3155.
- 628 37. Armstrong, R.; Brodzik, M. J.; Varani, A. The NSIDC EASE-Grid: Addressing the need
629 for a common, flexible, mapping and gridding scheme. *Earth Syst. Monit.* **1997**, *7*, 6–7.
- 630 38. Brodzik, M. J.; Knowles, K. EASE-Grid: A Versatile Set of Equal-Area Projections and
631 Grids. In *Discrete Global Grids*; 2002; p. Chapter 5.
- 632 39. Kerr, Y.; Jacquette, E.; Al Bitar, A.; Cabot, F.; Mialon, A.; Richaume, P.; Quesney, A.;
633 Berthon, L. *CATDS SMOS L3 soil moisture retrieval processor Algorithm Theoretical Baseline*
634 *Document (ATBD)*; 2013.
- 635 40. Jacquette, E.; Al Bitar, A.; Mialon, A.; Kerr, Y.; Quesney, A.; Cabot, F.; Richaume, P.
636 SMOS CATDS level 3 global products over land. *Remote Sens. Agric. Ecosyst. Hydrol. Xii* **2010**,
637 *7824*, 78240K–78240K–6.
- 638 41. Oliva, R.; Daganzo-Eusebio, E.; Kerr, Y. H.; Mecklenburg, S.; Nieto, S.; Richaume, P.;
639 Gruhier, C. SMOS radio frequency interference scenario: Status and actions taken to improve the RFI
640 environment in the 1400-1427-MHZ passive band. *IEEE Trans. Geosci. Remote Sens.* **2012**, *50*,

641 1427–1439.

642 42. Khazaal, A.; Anterrieu, E.; Cabot, F.; Kerr, Y. H. Impact of Direct Solar Radiations Seen
643 by the Back-Lobes Antenna Patterns of SMOS on the Retrieved Images. *IEEE J. Sel. Top. Appl. Earth*
644 *Obs. Remote Sens.* **2016**, 1–8.

645 43. Wang, J. R.; Choudhury, B. J. Remote sensing of soil moisture content, over bare field at
646 1.4 GHz frequency. *J. Geophys. Res.* **1981**, *86*, 5277.

647 44. Escorihuela, M. J.; Kerr, Y. H.; De Rosnay, P.; Wigneron, J. P.; Calvet, J. C.; Lemaître,
648 F. A simple model of the bare soil microwave emission at L-band. *IEEE Trans. Geosci. Remote Sens.*
649 **2007**, *45*, 1978–1987.

650 45. Lawrence, H.; Wigneron, J.-P.; Demontoux, F.; Mialon, A.; Kerr, Y. H. Evaluating the
651 Semiempirical H– Q Model Used to Calculate the L-Band Emissivity of a Rough Bare Soil. *IEEE*
652 *Trans. Geosci. Remote Sens.* **2013**, *51*, 4075–4084.

653 46. Fernandez-Moran, R.; Wigneron, J. P.; Lopez-Baeza, E.; Al-Yaari, A.; Coll-Pajaron, A.;
654 Mialon, A.; Miernecki, M.; Parrens, M.; Salgado-Hernanz, P. M.; Schwank, M.; Wang, S.; Kerr, Y.
655 H. Roughness and vegetation parameterizations at L-band for soil moisture retrievals over a vineyard
656 field. *Remote Sens. Environ.* **2015**, *170*, 269–279.

657 47. Ulaby, F. T.; Moore, R. K.; Fung, A. K. *Microwave Remote Sensing: Active and Passive*
658 *Volume II: Radar Remote Sensing and Surface Scattering and Emission Theory*; 1982; Vol. 2.

659 48. Mironov, V.; Kerr, Y.; Member, S.; Wigneron, J.; Member, S. Temperature- and Texture-
660 Dependent Dielectric Model for Moist Soils at 1.4 GHz. **2012**, *10*, 1–5.

661 49. Masson, V.; Champeaux, J. L.; Chauvin, F.; Meriguet, C.; Lacaze, R. A global database
662 of land surface parameters at 1-km resolution in meteorological and climate models. *J. Clim.* **2003**,
663 *16*, 1261–1282.

664 50. Fao *Digital Soil Map of the World and derived soil properties (CD-ROM)*; 1998.

665 51. Berrisford, P.; Kållberg, P.; Kobayashi, S.; Dee, D.; Uppala, S.; Simmons, A. J.; Poli, P.;
666 Sato, H. Atmospheric conservation properties in ERA-Interim. *Q. J. R. Meteorol. Soc.* **2011**, *137*,
667 1381–1399.

668 52. Wigneron, J.-P.; Laguerre, L.; Kerr, Y. H. A simple parameterization of the L-band
669 microwave emission from rough agricultural soils. *IEEE Trans. Geosci. Remote Sens.* **2001**, *39*,
670 1697–1707.

671 53. Al-Yaari, A.; Wigneron, J. P.; Ducharne, A.; Kerr, Y.; de Rosnay, P.; de Jeu, R.; Govind,
672 A.; Al Bitar, A.; Albergel, C.; Muñoz-Sabater, J.; Richaume, P.; Mialon, A. Global-scale evaluation
673 of two satellite-based passive microwave soil moisture datasets (SMOS and AMSR-E) with respect

- 674 to Land Data Assimilation System estimates. *Remote Sens. Environ.* **2014**, *149*, 181–195.
- 675 54. Albergel, C.; Dorigo, W.; Balsamo, G.; Muñoz-Sabater, J.; de Rosnay, P.; Isaksen, L.;
676 Brocca, L.; de Jeu, R.; Wagner, W. Monitoring multi-decadal satellite earth observation of soil
677 moisture products through land surface reanalyses. *Remote Sens. Environ.* **2013**, *138*, 77–89.
- 678 55. Leroux, D. J.; Kerr, Y. H.; Bitar, A. Al; Bindlish, R.; Member, S.; Jackson, T. J.; Berthelot,
679 B.; Portet, G. Comparison Between SMOS , VUA , ASCAT, and ECMWF soil moisture products
680 over four watersheds in US. **2014**, *52*, 1562–1571.
- 681 56. Albergel, C.; de Rosnay, P.; Gruhier, C.; Muñoz-Sabater, J.; Hasenauer, S.; Isaksen, L.;
682 Kerr, Y.; Wagner, W. Evaluation of remotely sensed and modelled soil moisture products using global
683 ground-based in situ observations. *Remote Sens. Environ.* **2012**, *118*, 215–226.
- 684 57. Louvet, S.; Pellarin, T.; al Bitar, A.; Cappelaere, B.; Galle, S.; Grippa, M.; Gruhier, C.;
685 Kerr, Y.; Lebel, T.; Mialon, A.; Mougouin, E.; Quantin, G.; Richaume, P.; de Rosnay, P. SMOS soil
686 moisture product evaluation over West-Africa from local to regional scale. *Remote Sens. Environ.*
687 **2015**, *156*, 383–394.
- 688 58. De Jeu, R. a. M.; Owe, M. Further validation of a new methodology for surface moisture
689 and vegetation optical depth retrieval. *Int. J. Remote Sens.* **2003**, *24*, 4559–4578.
- 690 59. Andela, N.; Liu, Y. Y.; M. Van Dijk, A. I. J.; De Jeu, R. A. M.; McVicar, T. R. Global
691 changes in dryland vegetation dynamics (1988-2008) assessed by satellite remote sensing: Comparing
692 a new passive microwave vegetation density record with reflective greenness data. *Biogeosciences*
693 **2013**, *10*, 6657–6676.
- 694 60. Dorigo, W. a.; Xaver, a.; Vreugdenhil, M.; Gruber, a.; Hegyiová, a.; Sanchis-Dufau,
695 a. D.; Zamojski, D.; Cordes, C.; Wagner, W.; Drusch, M. Global Automated Quality Control of In
696 Situ Soil Moisture Data from the International Soil Moisture Network. *Vadose Zo. J.* **2013**, *12*,
697 vj2012.0097.
- 698 61. Albergel, C.; de Rosnay, P.; Balsamo, G.; Isaksen, L.; Muñoz-Sabater, J. Soil Moisture
699 Analyses at ECMWF: Evaluation Using Global Ground-Based In Situ Observations. *J.*
700 *Hydrometeorol.* **2012**, *13*, 1442–1460.
- 701 62. Koster, R. D.; Guo, Z. C.; Yang, R. Q.; Dirmeyer, P. A.; Mitchell, K.; Puma, M. J. On
702 the Nature of Soil Moisture in Land Surface Models. *J. Clim.* **2009**, *22*, 4322–4335.
- 703 63. Escorihuela, M. J.; Chanzy, A.; Wigneron, J. P.; Kerr, Y. H. Effective soil moisture
704 sampling depth of L-band radiometry: A case study. *Remote Sens. Environ.* **2010**, *114*, 995–1001.
- 705 64. Njoku, E. G.; Kong, J.-A. Theory for passive microwave remote sensing of near-surface
706 soil moisture. *J. Geophys. Res.* **1977**, *82*, 3108.

- 707 65. Sheffield, J.; Goteti, G.; Wen, F.; Wood, E. F. A simulated soil moisture based drought
708 analysis for the United States. *J. Geophys. Res. D Atmos.* **2004**, *109*, 1–19.
- 709 66. Fan, Y.; van den Dool, H. Climate Prediction Center global monthly soil moisture data
710 set at 0.5° resolution for 1948 to present. *J. Geophys. Res. D Atmos.* **2004**, *109*.
- 711 67. Mahmoodi, A.; Richaume, P.; Kerr, Y.; Mialon, A.; Bircher, S.; Leroux, D. Evaluation
712 of MODIS IGBP land cover data on the SMOS Level 2 Soil Moisture Retrievals. In *Personal*
713 *communication*; Madrid, 2015.
- 714 68. Saleh, K.; Wigneron, J. P.; De Rosnay, P.; Calvet, J. C.; Kerr, Y. Semi-empirical
715 regressions at L-band applied to surface soil moisture retrievals over grass. *Remote Sens. Environ.*
716 **2006**, *101*, 415–426.
- 717 69. Ferrazzoli, P.; Guerriero, L.; Wigneron, J. P. Simulating L-band emission of forests in
718 view of future satellite applications. *IEEE Trans. Geosci. Remote Sens.* **2002**, *40*, 2700–2708.
- 719 70. Grant, J. P.; Saleh-Contell, K.; Wigneron, J.-P.; Guglielmetti, M.; Kerr, Y. H.; Schwank,
720 M.; Skou, N.; Van de Griend, A. a Calibration of the L-MEB model over a coniferous and a
721 deciduous forest. *IEEE Trans. Geosci. Remote Sens.* **2008**, *46*, 808–818.
- 722 71. Lawrence, H.; Wigneron, J. P.; Richaume, P.; Novello, N.; Grant, J.; Mialon, A.; Al Bitar,
723 A.; Merlin, O.; Guyon, D.; Leroux, D.; Bircher, S.; Kerr, Y. Comparison between SMOS Vegetation
724 Optical Depth products and MODIS vegetation indices over crop zones of the USA. *Remote Sens.*
725 *Environ.* **2014**, *140*, 396–406.



© 2017 by the authors; licensee Preprints, Basel, Switzerland. This article is an open access article distributed under the terms and conditions of the Creative Commons by Attribution (CC-BY) license (<http://creativecommons.org/licenses/by/4.0/>).